Pergamon

Int. J. Solids Structures Vol. 32, No. 17/18, pp. 2591–2607, 1995

0020-7683/95 $9.50 + .00

0020-7683(94)00284-3

DYNAMIC MIXED MODE FRACTURE OF CONCRETE

Z. K. GUO and A. S. KOBAYASHI
University of Washington, Department of Mechanical Engineering, Seattle, WA 98195, U.S.A.

and

N. M. HAWKINS
University of Illinois at Urbana-Champaign, Department of Civil Engineering, Urbana, IL 61801-2397, U.S.A.

(*Received* 3 *February* 1994)

Abstract—The transient moiré fringe patterns surrounding a rapidly propagating crack in an impacted three-point bend concrete specimen with an offset precrack were recorded by two IMACON 790 ultra-high speed framing cameras. The fracture parameters associated with this mixed mode fracture event were determined by driving a dynamic finite element model of the concrete specimen in its application mode with the recorded load and the crack propagation histories. The fracture process zone (FPZ), which trails the rapidly propagating crack, was characterized and the mixed modes I and II dynamic stress intensity factors were determined. The fracture energy dissipated at the FPZ increased with crack extension and reached a constant dissipation rate toward the final phase of fracture. Under mixed mode loading, the crack kinked and propagated according to the Ramulu–Kobayashi criterion.

INTRODUCTION

Impact resistance of concrete was initially quantified by the number of impacts to failure in a drop weight tester (Nanda and Hannant, 1969). The ACI Committee 544 on fiber-reinforced concrete subsequently recommended (1978) the use of a drop-weight test for the impact test which was followed by an instrumented drop-weight test to estimate the energy absorbed in the dynamic fracture process. Mindess and Benton (1985) and Bentur *et al.* (1986) used a large-scale drop-weight test method combined with high-speed photography to study the dynamic fracture response of hardened cement paste and reinforced concrete. Their measured crack velocities of 75–115 m s^{-1} were much smaller than the theoretical terminal crack velocities, and increased impact velocity had little effect on the maximum load at failure but increased the absorbed impact energy. Gopalaratnam and Shah (1986), John *et al.* (1987) and John and Shah (1990) utilized a modified Charpy impact tester together with a KRAK gage to measure the terminal crack velocity which was considered a characteristic value of dynamic fracture of concrete. Reinhardt (1986) and Jawed *et al.* (1987) followed the pioneering research of Goldsmith *et al.* (1966) by using a split Hopkinson bar to test concrete at very high impact velocity for generating a strain rate of the order of 1000 s^{-1}.

While the dynamic fracture studies described above were based on static analysis of the dynamic event, Du *et al.* (1992) and Yon *et al.* (1991, 1992) were the first to analyze the dynamic fracture responses of impacted, single-edged notch (SEN), three point bend (TPB) concrete specimens using a dynamic finite element code to characterize the fracture process zone (FPZ), which trails the propagating crack, of Hillerborg (1983, 1985a,b). This inverse analysis was validated by the matches between the computed and the measured crack opening displacements (CODs) and the strains at isolated locations. A study of a series of displacement-controlled impact tests of the TPB specimen and the crack-line wedge-loaded, double cantilever beam (CLWL-DCB) specimens with different strain rates led Yon *et al.* (1991, 1992) to propose a singular FPZ model for concrete fracture. This singular FPZ model, which was verified by the measured parabolic COD profile, is a Griffith

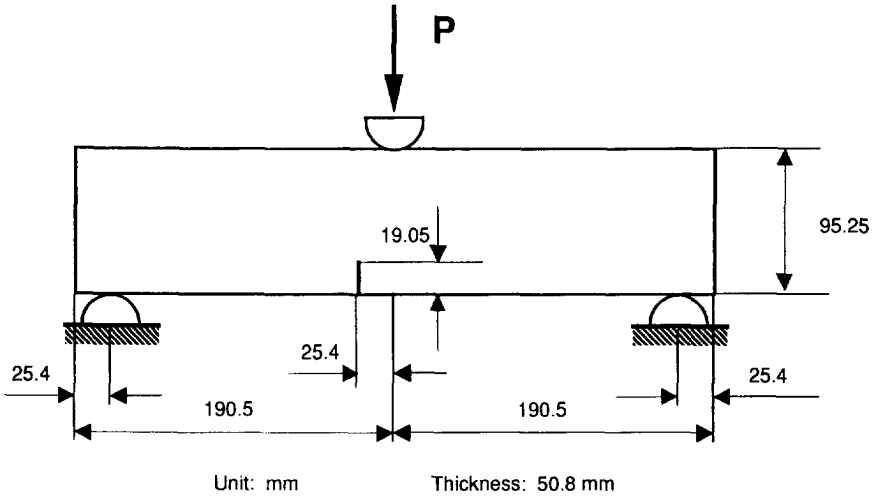

Fig. 1. SEN TPB concrete specimen.

crack with a trailing FPZ which reduced the COD and the stress intensity factor. Yon *et al.*'s inverse analysis also showed that the crack closing stress (CCS) versus COD relation was geometry and strain rate independent, but the dynamic stress intensity factor, K_I^{dyn}, was strain rate dependent.

The above-mentioned studies dealt only with mode I dynamic fracture. While mixed mode static fracture has been studied extensively by, among others, Bazant and Gambarova (1980, 1984) and Bazant and Lin (1988), very few papers on mixed mode dynamic fracture of concrete have been published to date. These include Shah and John (1986), John and Shah (1990) and Yu *et al.* (1994), all of whom used an impacted TPB specimen with an offset precrack. While John and Shah (1990) did not evaluate their experimental data by a dynamic analysis, Yu *et al.* (1994) used a dynamic finite element code to evaluate their dynamic moiré interferometry data. A CCS versus COD relation was obtained by matching the computed COD and CSD with their measured counterpart and the CSS versus the CSD relation was found to be insignificant in this mixed mode fracture. Also the energy rates were computed from the finite element analysis output.

The objective of this paper is to present new results on the mixed mode dynamic fracture of concrete where, unlike the experiments of Yu *et al.* (1994), the two orthogonal transient displacement fields were recorded simultaneously by an improved experimental technique, and the load-line displacement, which provided another check point in the inverse analysis, was measured.

EXPERIMENTAL PROCEDURES

Specimen

The SEN TPB concrete specimen used in this study is shown in Fig. 1. The concrete consists of a high early-strength Portland cement (type III), local sand, aggregate and water mixed in the proportion 1 : 3 : 2 : 0.5, respectively. The average gradation of the sand was based on ASTM C-404 Size No. 1 specifications and the maximum gravel size was 6.4 mm. Three days before the test, a notch 19 mm deep and 0.26 mm thick with an offset distance of 25.4 mm was machined in the specimen by a diamond saw. The day before testing, a moiré diffraction grating, which yielded horizontal and vertical displacements in a 95×95 mm field of 600 lines mm^{-1}, was transferred to the polished specimen surface and five strain gages were installed on the other unpolished surface along the predicted crack path. The initial machined crack was then extended by stable crack growth for about an additional 13 mm depth by subjecting the specimen to a TPB loading symmetric to the machined notch. The crack tip location in this precracking process was monitored by moiré interferometry.

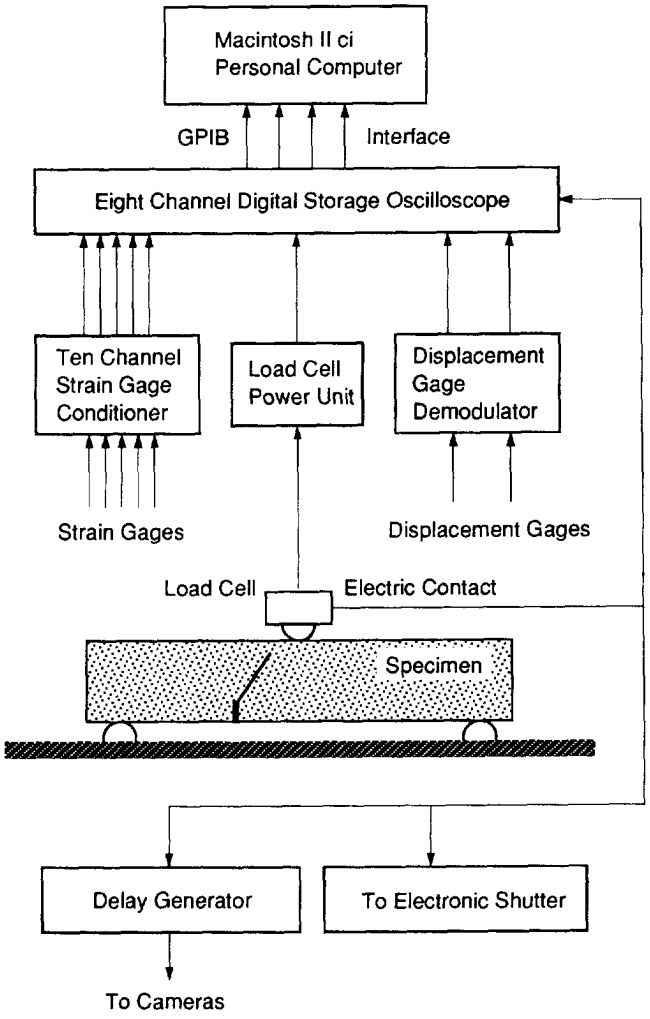

Fig. 2. Schematic of instrumentation of dynamic testing system.

Test procedure

A specially constructed drop-weight tester with a 10 kg impactor weight and a maximum drop height of about 1 m was used to generate a high strain rate dynamic loading. A rubber pad was placed between the impactor and the specimen in order to reduce the inertial effect on the measured load (Suaris and Shah, 1981, 1984). The concrete specimen was instrumented with a dynamic load cell at the contact point, two non-contact displacement gages at the load point on both sides of the specimen and five strain gages. The two displacement gages provided average load-line displacement data and accounted for the uneven crush of the specimen at the impact point. The five strain gage data provided an estimate of the crack velocity. Figure 2 shows a schematic of the instrumentation. Upon contact with the push rod, the drop-weight triggered the oscilloscope and an acousto-optic modulator. The trigger signal to the cameras was delayed at varying time intervals to record the dynamic fracture process at various crack lengths.

A four-beam moiré interferometer was used to measure simultaneously the two orthogonal u_x and u_y displacement fields on the front surface of the specimen. Separation of the two u_x and u_y displacement fields was accomplished by a slight tilt in one of the incident light beams such that the exit beam focused on a different spot from the other beam. Two mirrors deflect the two beams into two IMACON 790 cameras for simultaneous recording of the u_x and u_y displacements. Alternatively, the two beams can be redirected into a single camera to provide a side-by-side photograph of the two moiré fringe patterns as per Dadkhah *et al.* (1988). This procedure was also successfully used to record the two u_x and

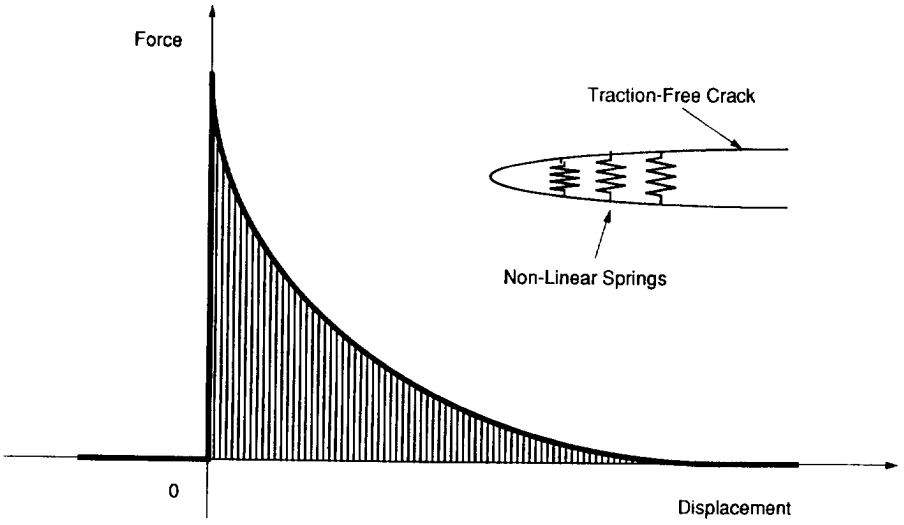

Fig. 3. Force–displacement relation for non-linear springs.

u_y moiré patterns simultaneously. The two cameras were triggered at a selected delay time at a rate of 100,000 frames s^{-1} and provided eight frames at an exposure time of 2 μs per frame. The total fracture event, which lasted about 1.5 ms, was obtained by assembling a composite record of four dynamic tests of identical fracture specimens with varying time delays to trigger the cameras.

NUMERICAL MODELING

In this study, a finite element analysis was used to model the static and dynamic crack propagation in concrete fracture specimens. The experimental data drove a dynamic finite element code and the CCS versus COD and the CSS versus CSD relations governing the FPZ were extracted. Fracture parameters, such as energy release and dissipation rates and stress intensity factors, were also computed from the finite element output using the application phase of the hybrid experimental–numerical analysis. The starting point of this application analysis was the fracture properties determined previously (Guo *et al.*, 1994) to predict the experimental results, such as the load, the load-line displacement, the COD and the CSD, and the strain history. The non-linear fracture behavior in the FPZ was adequately simulated by a commercial code (Gylltoft, 1991) using either the discrete or the smeared model. In the discrete approach, stress transfer in the FPZ was modeled by non-linear springs. The springs acting perpendicular to the crack were used to model the opening mode, i.e. mode I fracture, and springs parallel to the crack were used to model the sliding mode, i.e. mode II fracture. The assumed CCS versus COD and the CSS versus CSD relations were used to define the force–displacement relation for non-linear springs. Figure 3 shows a force–displacement curve of the non-linear spring for mode I fracture. For mixed mode simulation, a double noding technique (Liaw *et al.*, 1984) was used. In the smeared approach, the crack was modeled by using the build-in "CONCRETE" option of ABAQUS.

Numerical procedures for FPZ characterization

Figure 4 shows the finite element mesh for the SEN TPB specimen. The entire specimen had to be modeled for the mixed mode fracture analysis because of the asymmetry of the geometry and boundary conditions as in the previous analysis by Liaw *et al.* (1990). Both regular four-node quadrilateral elements and three-node triangle elements were used. This finite element model was numerically calibrated with known fracture mechanics solutions for accurate determination of the fracture parameters using the static, SEN TPB solution (Tada *et al.*, 1973) and the solution for a constant velocity crack in an infinite solid (Broberg, 1960).

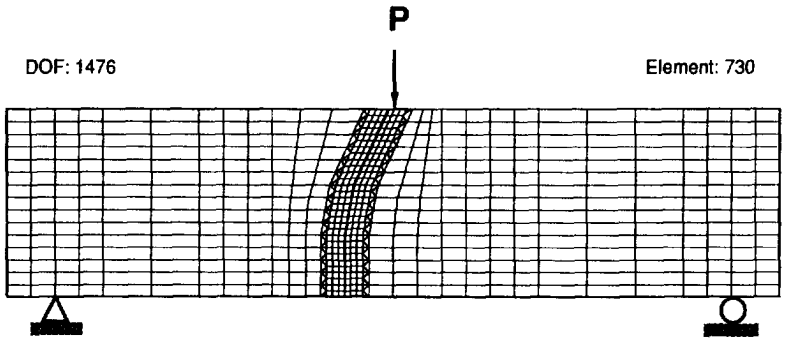

Fig. 4. Finite element mesh for dynamic mixed mode fracture.

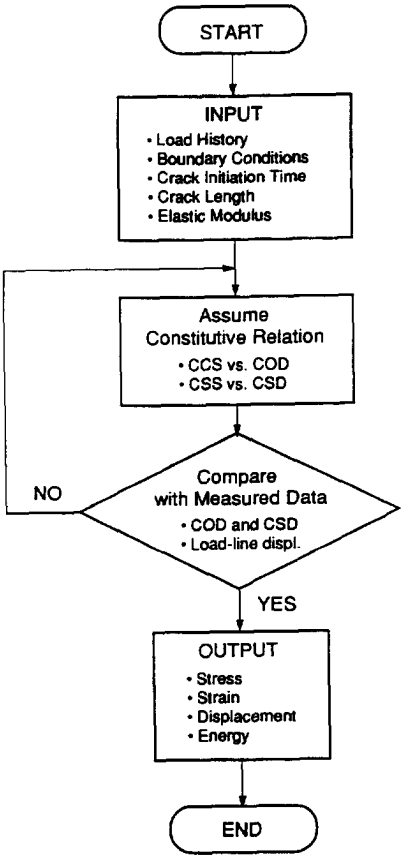

Fig. 5. Flow chart of numerical procedure.

Figure 5 shows the flow diagram of the numerical procedure used in this study. Unlike the direct analysis for static mode I fracture by Guo *et al.* (1991a,b), a time consuming inverse analysis (Du *et al.*, 1992; Liaw *et al.*, 1990; Yon *et al.*, 1992) was used here since the relative displacement fields obtained from moiré interferometry did not provide sufficiently accurate displacement data for prescribing a displacement boundary condition along the kinked crack. The input conditions for the application analysis were the experimentally determined dynamic loading history, boundary conditions, elastic modulus, crack velocity, crack initiation time and the instantaneous crack length together with the assumed CCS versus COD relation and the CSS versus CSD relations in the FPZ. Through a trial-and-error process, the optimized relations were obtained by matching the computed COD and CSD at every increment of crack extension with its measured counterparts.

As in all inverse procedures, the uniqueness of the CCS versus COD relation in the FPZ is not guaranteed. The computed results were assumed correct within the region

where the computed strains at the five strain gage locations and the computed load-line displacement agree with its measured counterparts. Another validation check involved computing the kinetic, strain and fracture energies separately, and then comparing the sum of these three quantities with the total input work at each instance of the crack extension. The final validation check involved the internal consistency of the computed results and their convergence to the known static counterpart at a low strain rate. The numerical results, which include stresses and strains in the crack tip elements, load-line displacements, displacements along the crack surfaces and all energies, were output for determining the fracture parameters.

For the dynamic fracture, the energy release rate with the kinetic energy rate per unit thickness can be written, as

$$G = \frac{dW}{da} - \frac{dU}{da} - \frac{dT}{da}, \tag{1}$$

where W and U denote the external work done on the specimen and its elastic energy per unit thickness, respectively, while T is the kinetic energy per unit thickness.

Since the crack propagated dynamically, the static relation between energy release rate, G, and stress intensity factor, K, is no longer valid. Freund (1972) showed that the dynamic energy release rate G_I^{dyn} can be related to the dynamic stress intensity factor K_I^{dyn} through a crack speed-dependent relation given by:

$$G_I^{dyn} = \frac{1-\nu^2}{E}(K_I^{dyn})^2 A(V), \tag{2}$$

where C_1 and C_2 are the dilatational and distorsional wave velocities, respectively, V is the crack speed and $A(V)$ is a universal function of the crack speed given by:

$$A(V) = \frac{(V/C_2)^2[1-(V/C_1)^2]^{1/2}}{(1-\nu)\{4[1-(V/C_1)^2]^{1/2}[1-(V/C_2)^2]^{1/2} - [2-(V/C_2)^2]^2\}}. \tag{3}$$

For dynamic mixed mode fracture, K_I^{dyn} and K_{II}^{dyn} were separated by assuming that the ratio of these two dynamic stress intensity factors was equal to the COD/CSD ratio.

RESULTS

The static tensile strength, f_t, of concrete specimens at the time of the test was 3.14 MPa. f_t was estimated by $f_t = 0.54\sqrt{f'_c}$ MPa, where f'_c is the compressive strength obtained from compression cylinder testing. With impact loading, the crack kinked immediately and propagated diagonally towards the load point.

Four specimens, which are identified as MB3-2, MB3-8, MB3-10 and MB3-24, were used in the dynamic mixed mode fracture study. The loading and the load-line displacement histories for each specimen are plotted in Figs 6 and 7, respectively. The actual crack paths on both sides of the specimens are shown in Fig. 8. These results for the four specimens are in good agreement with each other. The averaged loading history and crack path, as indicated, were used as input boundary conditions for the finite element analysis.

The averaged strain gage data for the four specimens, which were measured from five strain gages located on the crack path, are shown in Fig. 9. When the crack tip penetrated through the strain gage, the strain approached infinity from which the crack tip location was determined. Also shown in Fig. 9 by symbols are the computed strains based on finite element analysis.

Typical sequences of horizontal and vertical moiré interferometry patterns associated with a dynamic crack propagating in specimen MB3-10 are shown in Figs 10 and 11, respectively. The dark "L" shape in the pictures is a calibration target. These two moiré

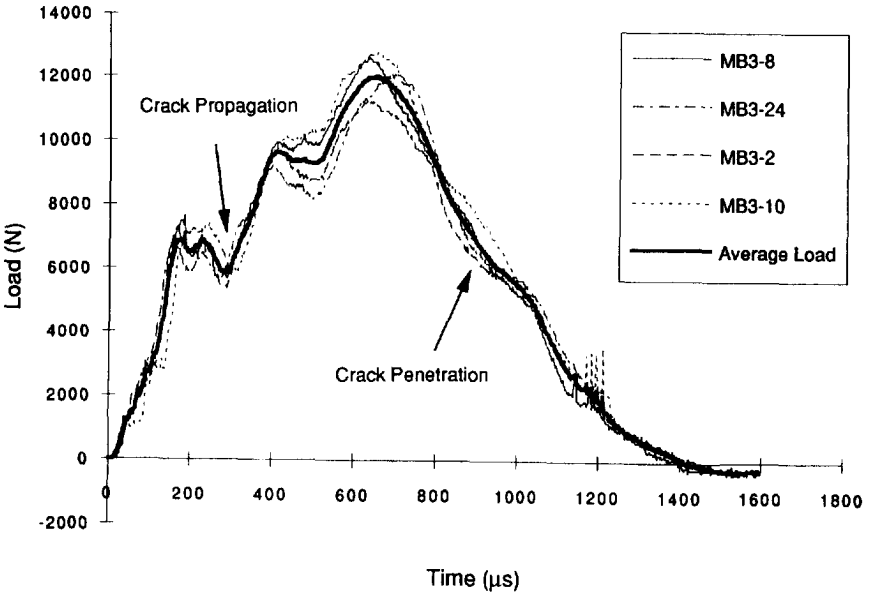

Fig. 6. Load histories of dynamic mixed mode concrete fracture tests.

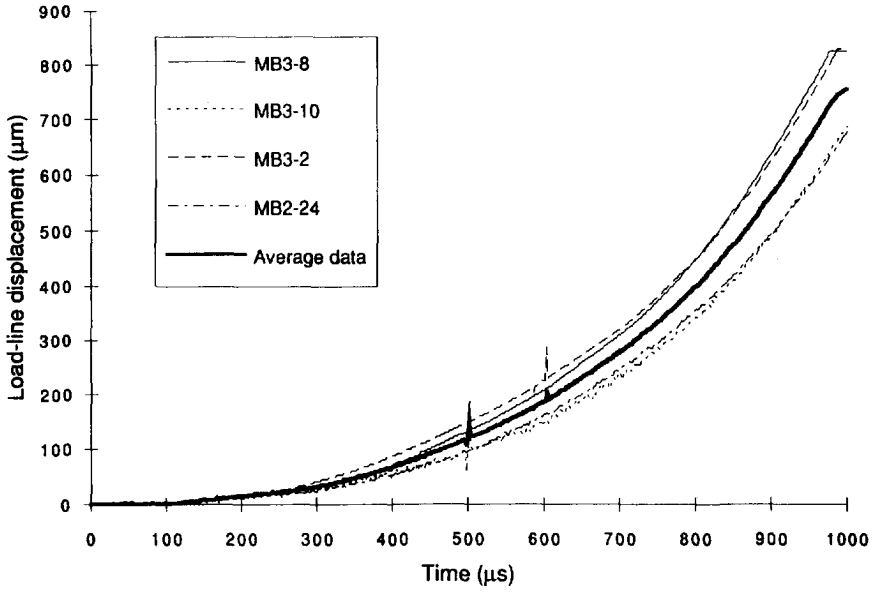

Fig. 7. Load-line displacements of dynamic mixed mode concrete fracture tests.

pictures were taken simultaneously by two synchronized IMACON 790 cameras. The time delay for triggering the cameras was 500 μs.

Figure 12 shows the crack length (a) variations with the time (t), where a is the length measured from the crack tip to the edge along the entire kinked crack paths of the four specimens. The circles and squares are the data obtained from the moiré pattern and the strain gage readings, respectively. The fitted curve of the crack length, which is shown in Fig. 12, was used in the numerical analysis. The crack velocity, which was determined from the curve, is shown in Fig. 13. The crack velocity reached a maximum after kinking and then decelerated as it approached the compression side of the TPB specimen. The maximum crack speed in those specimens was 178 m s^{-1}.

Figure 14 shows a composite picture of the variations in horizontal and vertical displacements, u_x and u_y, respectively, along the crack, obtained from the moiré patterns. Figure 14 also shows the computed u_x and u_y, which were generated by the finite element

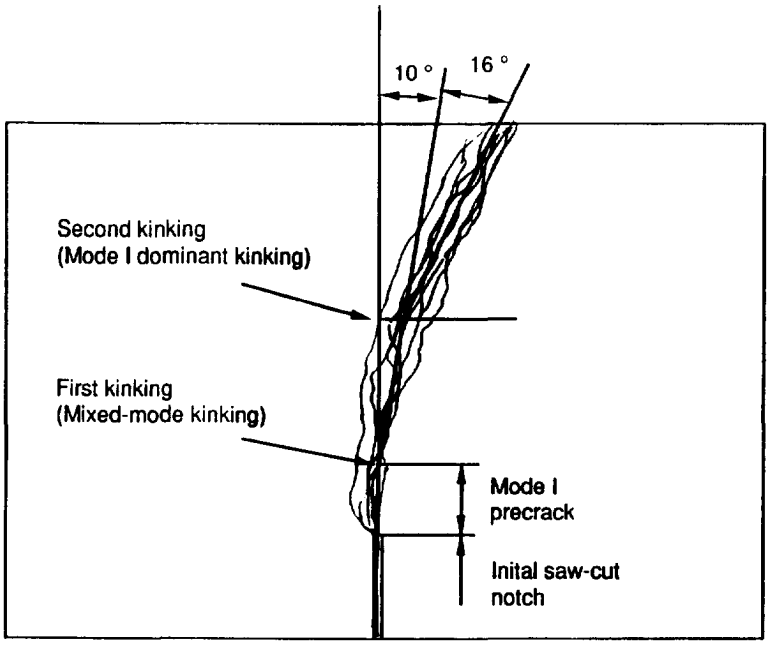

Fig. 8. Mixed mode crack paths.

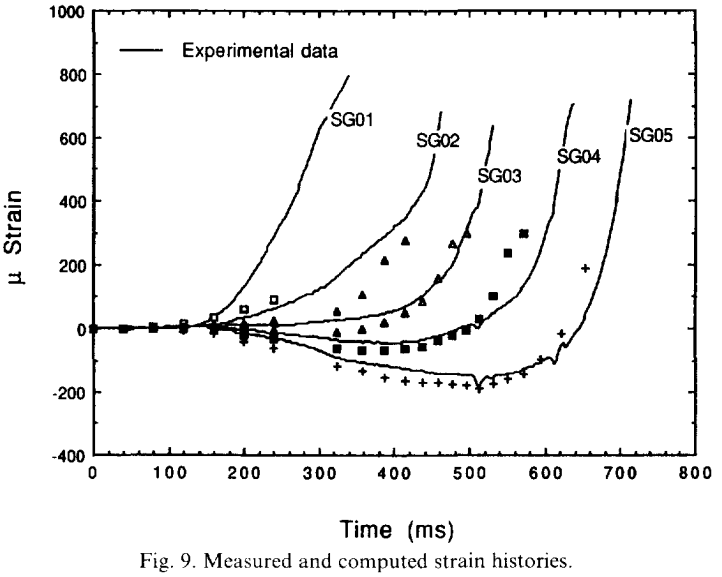

Fig. 9. Measured and computed strain histories.

analysis along the crack. The measured and computed values are in qualitative and quantitative agreements with each other.

Figure 15 shows the CCS versus COD relation for the dynamic mixed mode fracture of concrete specimens. This relation provides the best fit between the measured and computed displacement field around the crack tip as well as remote load-line displacement. Like the static mixed mode studies (Yu *et al.*, 1994), the CSS versus the CSD relation is missing in this figure and suggests that in the mixed mode dynamic fracture of concrete, aggregate interlocking can be ignored. Also shown for the comparison in Fig. 15 are the CCS versus COD relations for the static mode I and mixed mode fracture specimens, respectively.

Figure 16 shows sequences of COD and CSD distributions, respectively, which were computed from u_x and u_y through a coordinate transformation. The relatively constant CSD for the length of the initial straight crack indicates that the two free corners at the crack mouth of the single edge notch specimen were displacing relative to each other as a rigid body and are shear strain free.

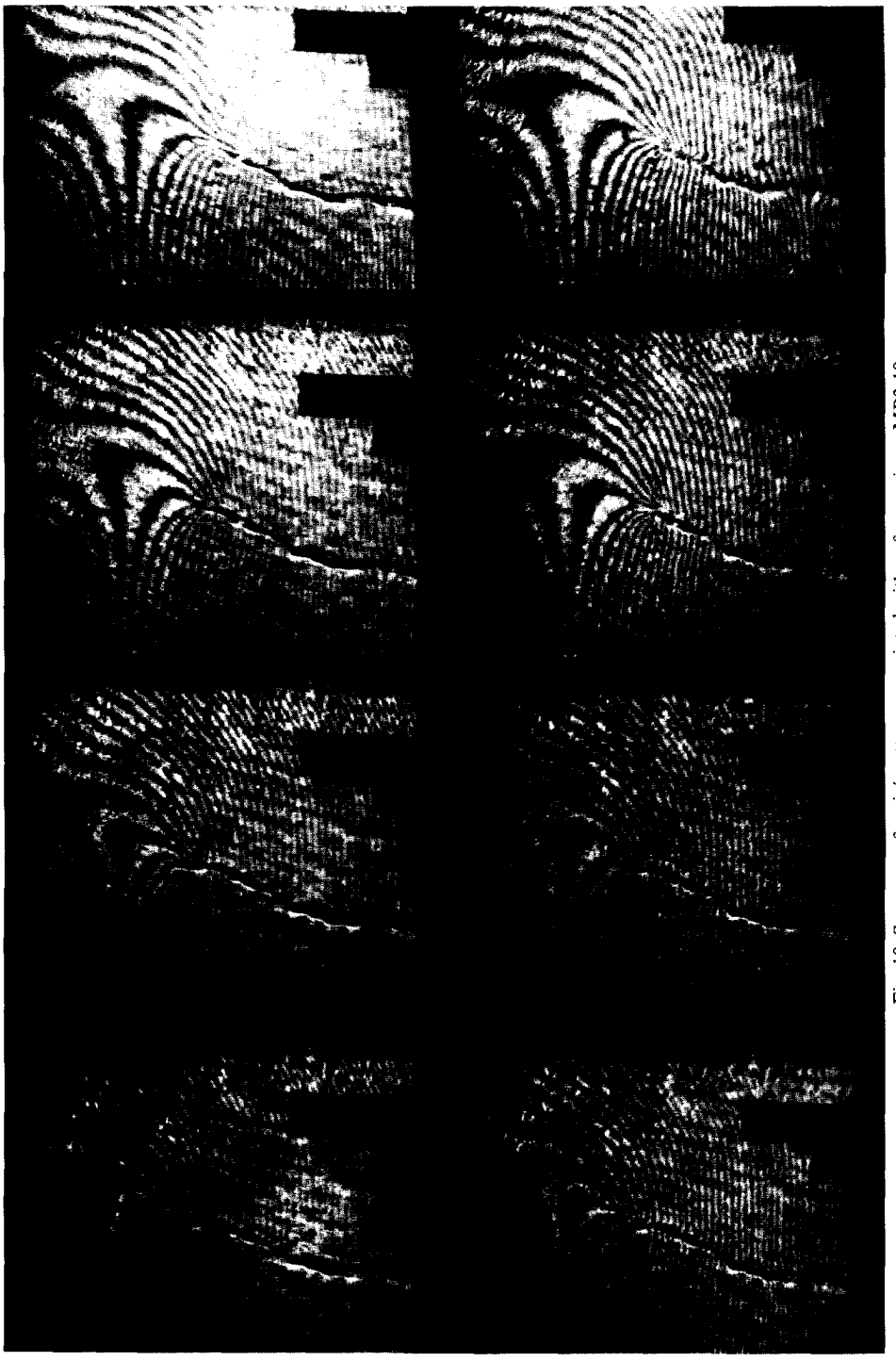

Fig. 10. Sequence of moiré patterns associated with u_y for specimen MB3-10.

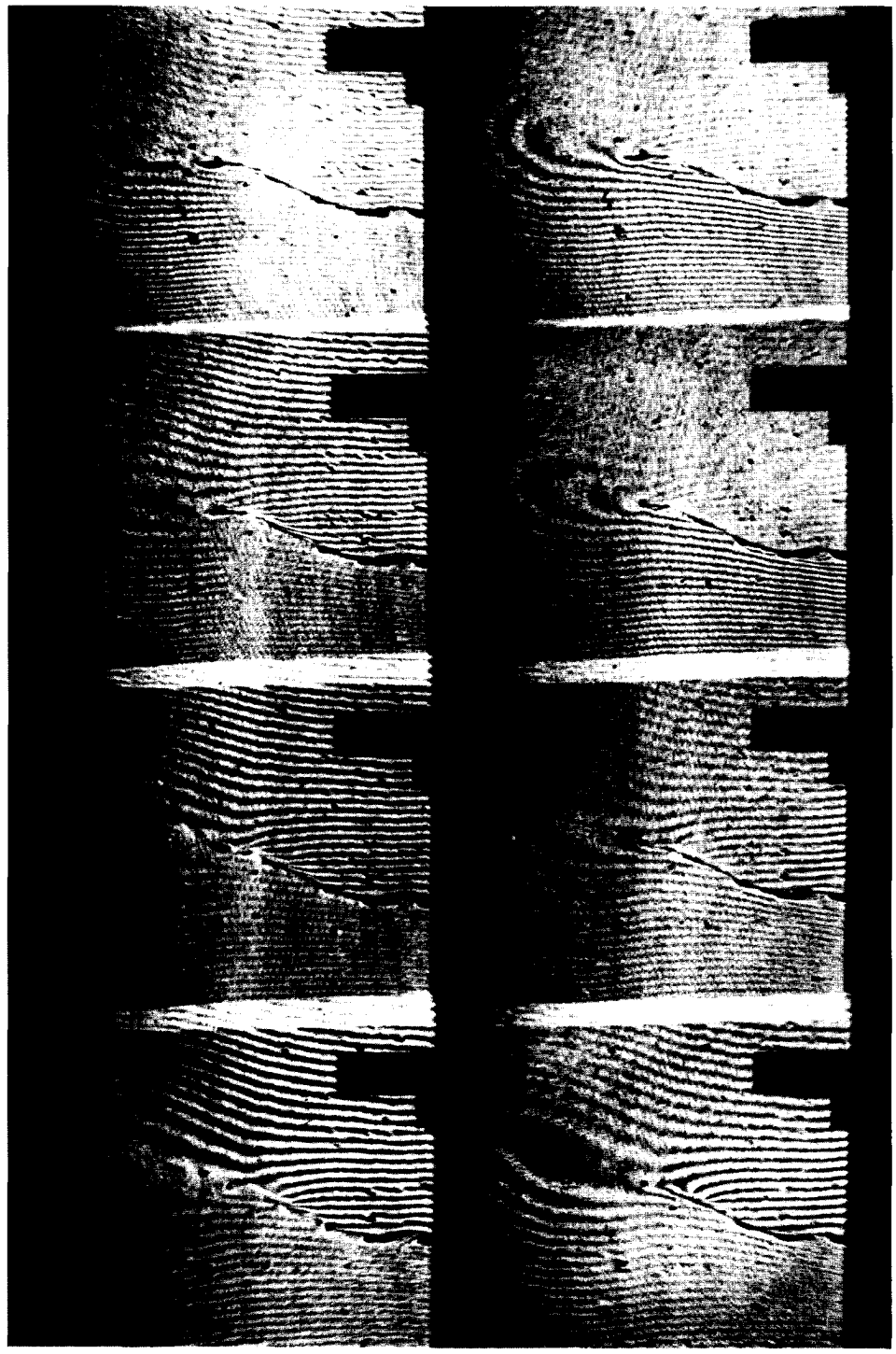

Fig. 11. Sequence of moiré patterns associated with u_x for specimen MB3-10.

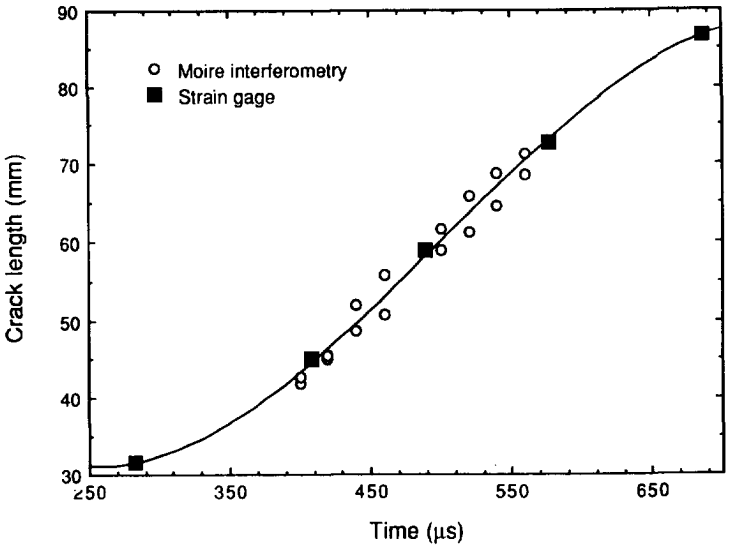

Fig. 12. Crack length variation with time.

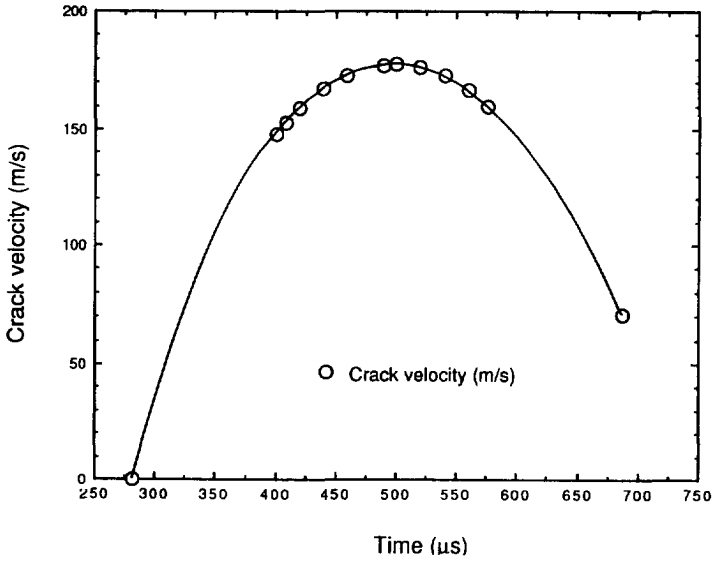

Fig. 13. Crack velocity variation with time.

Figure 17 shows the $K_{\mathrm{I}}^{\mathrm{dyn}}$ and $K_{\mathrm{II}}^{\mathrm{dyn}}$ variations with crack extensions. The $K_{\mathrm{I}}^{\mathrm{dyn}}$ and $K_{\mathrm{II}}^{\mathrm{dyn}}$ were calculated from the dynamic energy release rate of eqn (2). The $K_{\mathrm{I}}^{\mathrm{dyn}}$ value is consistently larger than the crack resistance, K_{IR}, as obtained in the static mode I test. $K_{\mathrm{II}}^{\mathrm{dyn}}$ is practically zero but changes sign at the second kinking.

Figure 18 shows the changes in energy partition with rapid and kinked crack extension. Unlike the situation for a somewhat ductile material, the kinetic energy is relatively large and is more characteristic of a brittle material. Figure 19 shows the energy rates obtained from Fig. 18.

VALIDATION

As in all inverse analyses, the uniqueness of the results is in doubt. Much of such uncertainty was removed by matching the computed and the measured u_x and u_y or the CODs and the CSDs. These crack tip parameters are more sensitive to changes in the FPZ than the remote parameters, such as load, load-line displacement and the crack mouth opening and sliding displacements. In fact, previous analysis showed that the computed

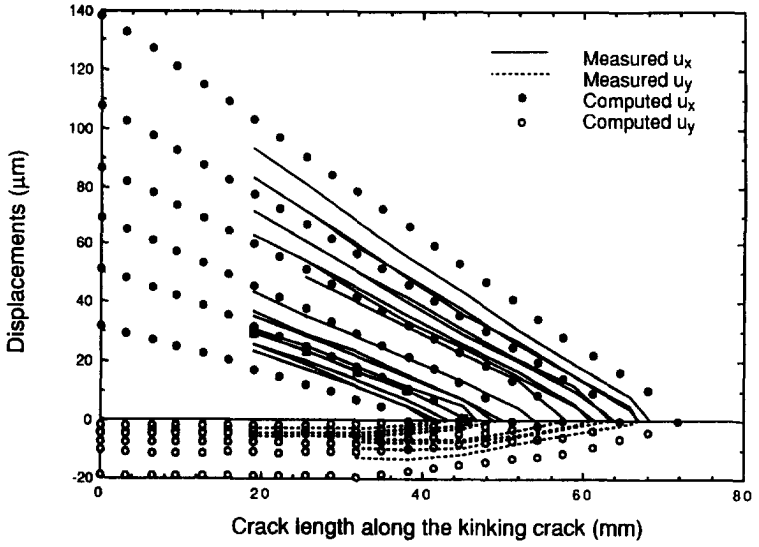

Fig. 14. Measured and computed u_x and u_y.

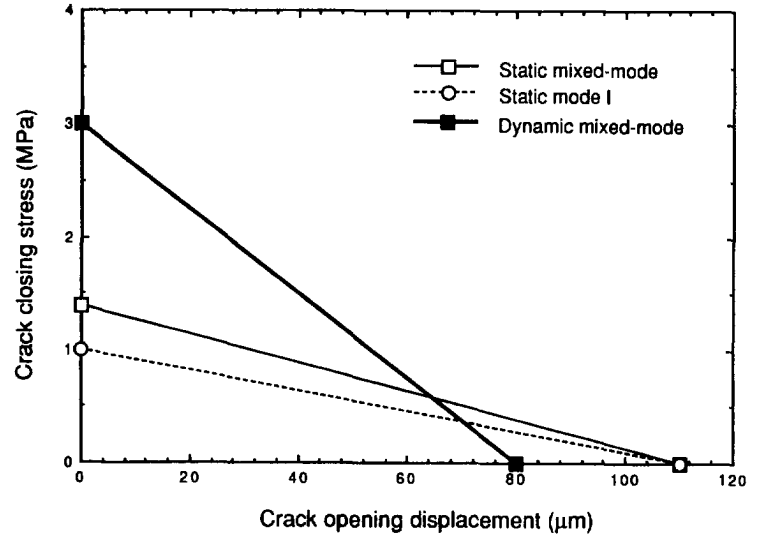

Fig. 15. CCS versus COD relation for the dynamic mixed mode fracture of concrete.

and measured u_x and u_y could be matched with a sizable CSS versus CSD relation. Therefore, more evidence was needed to support the reasonableness of the CCS versus COD relation in the FPZ. For this purpose, the crack kinking angle, the load-line displacement and the strain gage data were used to validate the results of this inverse analysis.

Crack kinking angle

In the mixed mode I and mode II fracture, Erdogan and Sih (1963) derived the maximum stress criterion, which is also identical with the maximum circumferential stress criterion, to predict the angle of crack kinking, θ_c in the presence of K_{II}. This maximizing condition yields

$$K_I \sin\theta_c + K_{II}(3\cos\theta_c - 1) = 0, \tag{4}$$

where K_I and K_{II} are the modes I and II stress intensity factors, respectively.

In the absence of K_{II}, however, eqn (4) predicts a self-similar crack propagation or $\theta_c = 0$ and fails to explain the physically observed crack instability where crack kinking takes place in a K_I field. The static elastic crack kinking criterion, which incorporates the

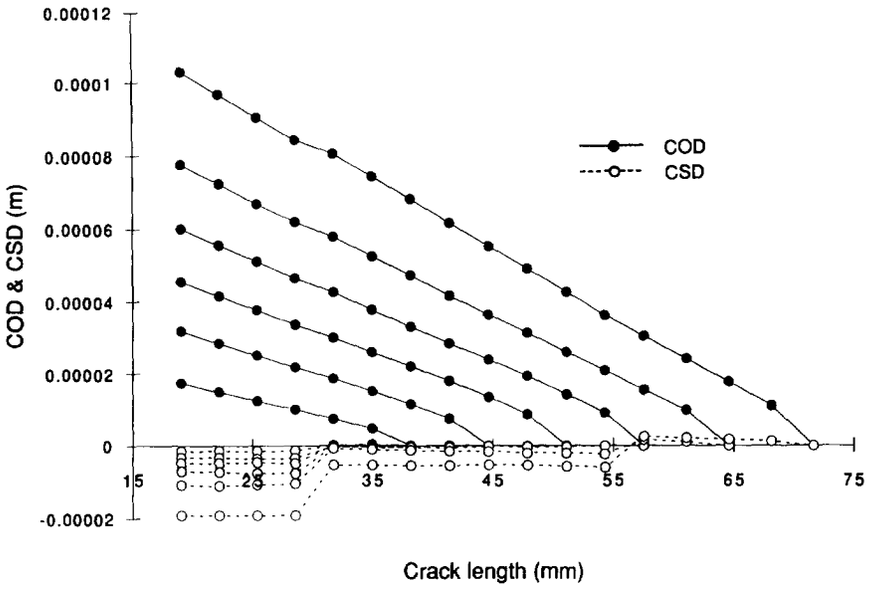

Fig. 16. Sequences of COD and CSD distributions.

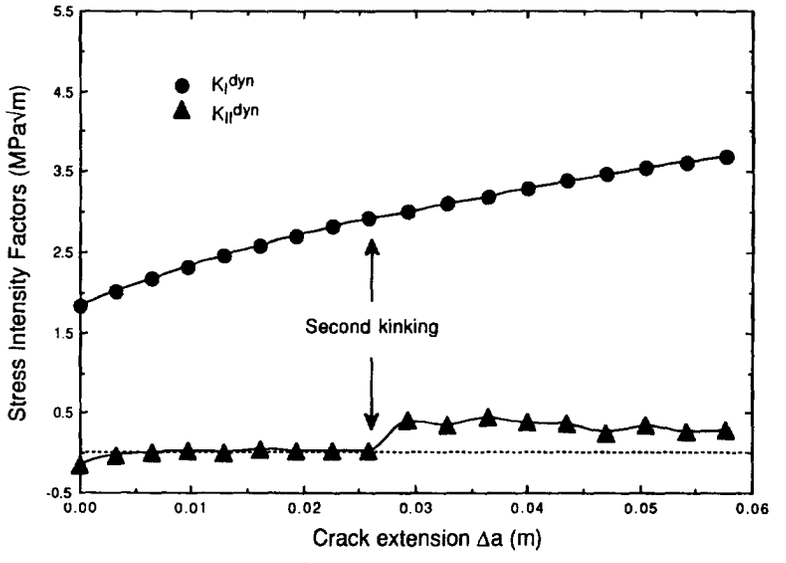

Fig. 17. K_I^{dyn} and K_{II}^{dyn} variations with the crack extension.

second order term in the crack tip stress field, of Streit and Finnie (1980) or the dynamic counterpart of Ramulu and Kobayashi (1983), predicts such crack kinking and was found to agree well with available experimental data.

In the mixed mode, the elastic crack tip stress field in terms of the crack tip polar coordinate system is given by

$$\sigma_{rr} = \frac{1}{\sqrt{(2\pi r)}}\cos\frac{\theta}{2}\left[K_I\left(1+\sin^2\frac{\theta}{2}\right)+\tfrac{3}{2}K_{II}\sin\theta-2K_{II}\tan\frac{\theta}{2}\right]+\frac{\sigma_{ox}}{2}(1+\cos 2\theta)$$

$$\sigma_{\theta\theta} = \frac{1}{\sqrt{(2\pi r)}}\cos\frac{\theta}{2}\left[K_I\cos^2\frac{\theta}{2}-\tfrac{3}{2}K_{II}\sin\theta\right]+\frac{\sigma_{ox}}{2}(1-\cos 2\theta)$$

$$\tau_{r\theta} = \frac{1}{2\sqrt{(2\pi r)}}\cos\frac{\theta}{2}[K_I\sin\theta+K_{II}(3\cos\theta-1)]-\frac{\sigma_{ox}}{2}\sin 2\theta, \tag{5}$$

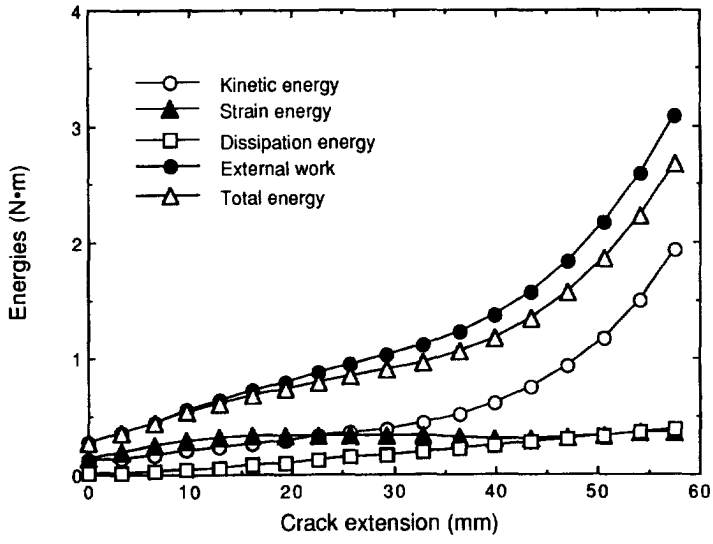

Fig. 18. Energy partitions with crack extension.

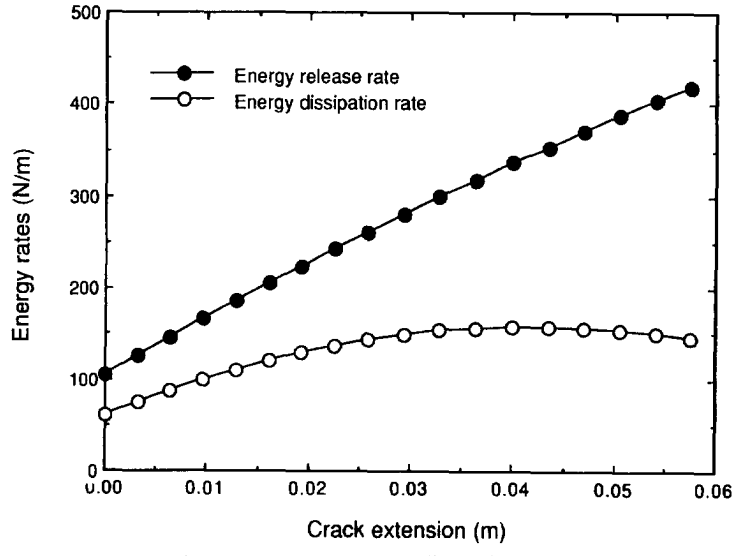

Fig. 19. Energy release and dissipation rates.

where σ_{ox} is the second order term and is commonly referred to as the remote stress component. The same maximum circumferential stress criterion is then used to derive a mixed mode crack extension criterion by assuming that fracture will occur when the maximum circumferential stress is equal to the equivalent circumferential stress in mode I fracture. Experimental evidence compiled by Ramulu and Kobayashi (1983) heavily favors the incorporation of the second order term in predicting the crack kinking angle under mixed mode fracture. The mixed mode fracture criterion of eqn (4) then becomes

$$K_{Ic} = K_I \cos^3\frac{\theta_c}{2} - 3K_{II}\cos^2\frac{\theta_c}{2}\sin\frac{\theta_c}{2} + \frac{\sqrt{(2\pi r_c)}}{2}\sigma_{ox}(1-\cos 2\theta_c), \tag{6}$$

where r_c is a material property.

The crack kinking angle can be obtained by maximizing the crack tip circumferential stress and results in the following transcendental equation:

Table 1. Measured and predicted first kinking angles

Measured kinking angle	10°
σ_{ox}	0.0183 MPa m
r_o	3.2 mm
K_{II}/K_I	−0.087
Predicted kinking angle (Ramulu and Kobayashi, 1983)	9.92°
Error	0.8%
Predicted kinking angle (Erdogan and Sih, 1963)	9.82°
Error	1.8%

Table 2. Predicted second kinking angles

Measured kinking angle	16°
σ_{ox}	5.77 MPa m$^{1/2}$
r_o	3 mm
r_c	3.2 mm
K_{II}/K_I	−0.0067
Predicted kinking angle	15.8°
Error	1.25%

$$\frac{K_{II}}{K_I} = \frac{-\sin(\theta_c/2)}{(3\cos\theta_c - 1)}\left[2\cos\frac{\theta_c}{2} - \frac{16\sqrt{(2\pi)}}{3}\cdot A\cdot\cos\theta_c\right] \tag{7}$$

$$A = \sqrt{r_c}\,\frac{\sigma_{ox}}{K_I}. \tag{8}$$

The term A is related to the critical distance r_c from the crack tip and is proportional to the non-singular stress, σ_{ox}. For a pure mode I crack tip stress field, Ramulu and Kobayashi (1983) have shown that r_c is a material-dependent parameter which must be determined experimentally. Thus, unlike the crack kinking criterion represented by eqn (4), the crack kinking angle computed by eqn (6) incorporates the second order term and represents the mixed mode extension of the crack kinking criterion by Streit and Finnie (1980) and Ramulu and Kobayashi (1983). The crack kinking angle, θ_c, increases with increasing σ_{ox} and negative σ_{ox} tends to stabilize the crack path.

Continuous crack curving under such conditions will require that

$$r_o = \frac{9}{128\pi}\left(\frac{K_I}{\sigma_{ox}}\right)^2 < r_c \tag{9}$$

and the crack curving angle, θ_c, is

$$\theta_c = \cos^{-1}\left[\frac{1 \pm \sqrt{[1 + (1024\pi/9)r_c(\sigma_{ox}/K_I)^2]}}{(512\pi/9)r_c(\sigma_{ox}/K_I)^2}\right]. \tag{10}$$

In the dynamic mixed mode fracture of concrete, the first crack kinking occurred in the presence of mixed mode I and mode II. The crack kinking angle as predicted by Ramulu and Kobayashi's criterion is shown in Table 1. Erdogan and Sih's maximum circumferential criterion also yields the same result. The measured and predicted angles are in good agreement.

After the first kinking, the crack propagates in the dominant mode I with a negligible K_{II}. In the absence of K_{II}, the second kinking occurred when Ramulu and Kobayashi's criterion was satisfied. The kinking angle can be predicted by eqn (7), and the result is shown in Table 2.

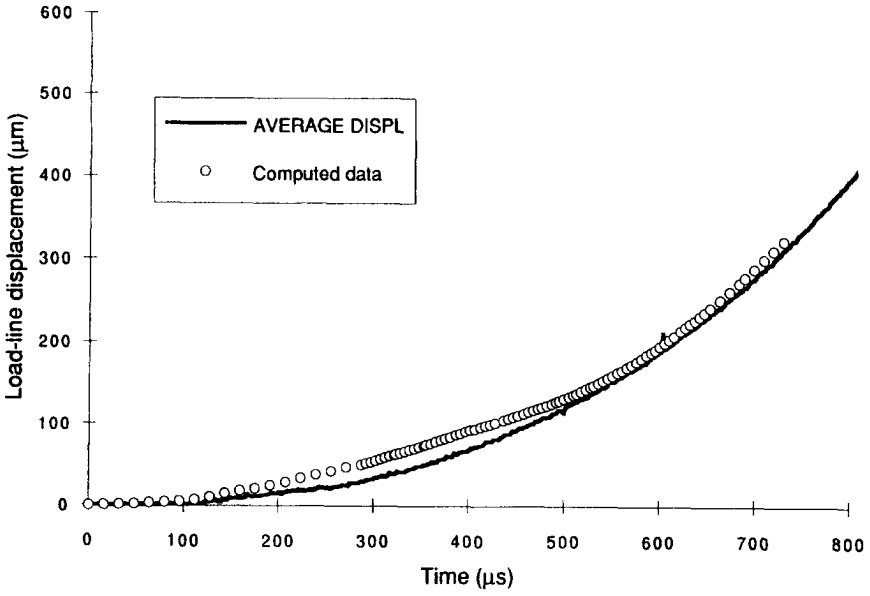

Fig. 20. Measured and computed load-line displacements.

Load-line displacement and strains

In order to reduce further the uncertainty of the inverse analysis, the load-line displacement and the strain gage data were used to validate the finite element model.

Figure 20 shows a superposed picture of the measured and the computed load-line displacements. The good agreement in this far field parameter also validates the accuracy of the finite element model.

Also shown in Fig. 9 are the measured and computed strains at the five strain gage locations. Some discrepancies between the measured and computed data, especially in the first strain gage, are noted. Since the strain gages were mounted before the static precracking procedure, the crack could have penetrated through the gage during the precracking process which could have caused these differences. Nevertheless, the general trend of those strain gage outputs match their computed counterparts.

CONCLUSIONS

The moiré interferometry technique was used successfully to determine the crack tip locations, the COD and the CSD. The technique for simultaneously recording the orthogonal displacement fields was developed for the dynamic fracture of concrete test. Together with the instrumentation, sufficient boundary conditions were obtained to drive the finite element code and then to validate the finite element model.

A two-dimensional finite element model was employed successfully to model the static and dynamic fracture of concrete. Experimental results can be predicted well by the finite element model. Fracture parameters, such as energy release and dissipation rates and stress intensity factors, were determined from the finite element output.

The CCS versus the COD relation can be modeled using a simple straight line model. This relation is very sensitive to the variations of the near field parameters, such as u_x and u_y, rather than the far field parameters, such as load and load-line displacement.

The crack kinking criteria can be applied to the concrete specimen. They play a very important role in validating the FPZ models.

Acknowledgements—This research was supported by Air Force Office of Scientific Research AFOSR-01-0218 and F49620-93-1-0210. The authors wish to thank Drs Spencer Wu and Walter F. Jones for their valuable advice during the course of this investigation.

REFERENCES

ACI Committee 544 (1978). Measurement of properties of fiber reinforced concrete. *J. Am. Concrete Inst.* **75,** 283–289.

Bazant, Z. P. and Gambarova, P. (1980). Rough cracks in reinforced concrete. *ASCE J. Struct. Engng* **106,** 819–842.

Bazant, Z. P. and Gambarova, P. (1984). Crack shear in concrete: crack band microplane model. *ASCE J. Struct. Engng* **110,** 2015–2035.

Bazant, Z. P. and Lin, F.-B. (1988). Nonlocal smeared cracking model for concrete fracture. *ASCE J. Struct. Engng* **114,** 2493–2510.

Bentur, A., Mindess, S. and Banthia, N. P. (1986). The fracture of reinforced concrete under impact loading. In *Cement-based Composites: Strain Rate Effects on Fracture* (Edited by S. Mindess and S. P. Shah), Vol. 64, pp. 225–234. Materials Research Society Symposia Proceedings.

Broberg, K. B. (1960). The propagation of a brittle crack. *Arkiv Fys.* **18,** 159–192.

Dadkhah, M. S., Wang, F. X. and Kobayashi, A. S. (1988). Simultaneous on-line measurement of orthogonal displacement fields by moiré interferometry. *Exp. Tech.* **12,** 28–30.

Du, J. J., Yon, J.-H., Hawkins, N. M., Arakawa, K. and Kobayashi, A. S. (1992). Fracture process zone for concrete for dynamic loading. *ACI Mater. J.* **89,** 252–258.

Erdogan, F. and Sih, G. C. (1963). On the crack extension in plates under plane loading and transverse shear. *ASME J. Basic Engng* **85,** 519–27.

Freund, L. B. (1972). Crack propagation in an elastic solid subjected to general loading—Part 1. Constant rate of extension. *J. Mech. Phys. Solids* **20,** 129–140.

Goldsmith, W., Polivka, M. and Yang, T. (1966). Dynamic behavior of concrete. *Exp. Mech.* **6,** 65–79.

Gopalaratnam, V. S. and Shah, S. P. (1986). Properties of steel fiber reinforced concrete subjected to impact loading. *J. Am. Concrete Inst.* **83,** 117–126.

Guo, Z. K., Kobayashi, A. S. and Hawkins, N. M. (1991a). Fracture process zone for mode I concrete fracture. In *Fracture of Engineering Materials and Structures* (Edited by S. H. Teoh and K. H. Lee), pp. 332–337. Elsevier Applied Science, Amsterdam.

Guo, Z. K., Kobayashi, A. S. and Hawkins, N. M. (1991b). Fracture energy dissipation mechanism of concrete. In *Fracture Mechanics: 23rd Symposium* (Edited by R. Chona). *ASTM STP* **1189,** 797–805.

Guo, Z. K., Kobayashi, A. S. and Hawkins, N. M. (1994). Mixed modes I and II concrete fracture—an experimental analysis. *ASME J. Appl. Mech.* **61,** 815–821.

Gylltoft, K. (1991). Fracture mechanics analysis using ABAQUS. In *Analysis of Concrete Structures by Fracture Mechanics* (Edited by L. Elfgren and S. P. Shah), pp. 152–159. Chapman and Hall.

Hillerborg, A. (1983). Analysis of one single crack. In *Fracture Mechanics of Concrete* (Edited by F. H. Wittmann), pp. 223–249. Elsevier, Amsterdam.

Hillerborg, A. (1985a). Results of three comparative test series for determining the fracture energy G_F of concrete. *Mater. Structures* **18,** 406–413.

Hillerborg, A. (1985b). The theoretical basis of a method to determine the fracture energy G_F of concrete. *Mater. Structures* **18,** 291–296.

Jawed, I., Childs, G., Ritter, A., Winzer, S., Johnson, T. and Barker, D. (1987). High-strain-rate behavior of hydrated cement pasts. *Cement Concrete Res.* **17,** 433–440.

John, R. and Shah, S. P. (1990). Mixed mode fracture of concrete subjected to impact loading. *ASCE J. Struct. Engng* **116,** 585–602.

John, R., Shah, S. P. and Jenq, Y. -S. (1987). A fracture model to predict the rate sensitivity of mode I fracture of concrete. *Cement Concrete Res.* **17,** 249–262.

Liaw, B. M., Jeang, F. L., Du, J. J., Hawkins, N. M. and Kobayashi, A. S. (1990). Fracture process zone for mixed mode concrete fracture. *ASCE J. Engng Mech.* **116,** 1560–1579.

Liaw, B. M., Kobayahsi, A. S. and Emery, A. F. (1984). Double noding technique for mixed mode crack propagation studies. *Int. J. Numer. Meth. Structures* **20,** 967–977.

Mindess, S. and Benton, A. (1985). A preliminary study of the fracture of concrete beam under impact loading using high speed photography. *Cement Concrete Res.* **15,** 474–484.

Nanda, V. K. and Hannant, D. J. (1969). Fiber reinforced concrete. *Concrete Bldg Concrete Pros.* XIW 179–181.

Ramulu, M. and Kobayashi, A. S. (1983). Dynamic crack curving—a photoelastic evaluation. *Exp. Mech.* **23,** 1–9.

Reinhardt, H. W. (1986). Strain rate effects on the tensile strength of concrete as predicted by thermodynamic and fracture mechanics models. In *Cement-based Composite: Strain Rate Effects on Fracture* (Edited by S. Mindess and S. P. Shah). Vol. 64, pp. 1–20. Materials Research Society Symposia Proceedings.

Shah, S. P., and John, R. (1986). Rate-sensitivity of mode I and mode II fracture of concrete. In *Cement-based composites: strain rate effects on fracture* (Edited by S. Mindess and S. P. Shah), Vol. 64, pp. 21–38. Materials Research Society Symposia Proceedings.

Streit, R. and Finnie, I. (1980). An experimental investigation of crack path directional stability. *Exp. Mech.* **20,** 17–23.

Suaris, W. and Shah, S. P. (1981). Initial effects in the instrumented impact testing of cementitious composites. *Cement, Concrete Aggregates* **3,** 77–83.

Suaris, W. and Shah, S. P. (1984). Rate-sensitive damage theory for brittle solids. *J. Engng Mech.* **110,** 985–997.

Tada, H., Paris, P. C. and Irwin, G. R. (1973). *Stress Analysis of Cracks Handbook*. Del Research Corporation, Hellertown, Pennsylvania.

Yon, J.-H., Hawkins N. M. and Kobayashi, A. S. (1991). Fracture process zone in dynamically loaded crack-line wedge-loaded, double-cantilever beam concrete specimens. *ACI Mater. J.* **88,** 470–479.

Yon, J.-H., Hawkins N. M. and Kobayashi, A. S. (1992). Strain rate sensitivity of concrete mechanical properties. *ACI Mater. J.* **89,** 146–153.

Yu, C.-T., Kobayashi, A. S. and Hawkins, N. M. (1994). Crack kinking under mixed mode dynamic fracture of concrete. *Fracture Mechanics: 25th Symposium, ASTM STP* **1220.** In press.